Separation and Purification Technology 380 (2026) 135378

Contents lists available at ScienceDirect

Separation and Purification Technology

journal homepage: www.elsevier.com/locate/seppur

Synergy of sulfate radical-driven oxidation with dynamic in situ Fe(III) coagulation for enhanced NOM precursor removal

Lap-Cuong Hua [a], Yosheng Lin [b], Thi Ngoc Anh Nguyen [b], Jr Lin Lin [c], Chihpin Huang [b,*]

[a] IHE-Delft Institute for Water Education, Water Supply, Sanitation and Environmental Engineering Department, Westvest 7, 2611 AX Delft, the Netherlands
[b] Institute of Environmental Engineering, National Yang-Ming Chiao Tung University, Hsinchu 300, Taiwan, ROC
[c] Department of Civil Engineering, Chung Yuan Christian University, Chung-Li, Taiwan, ROC

ARTICLE INFO

Keywords:
NOM precursor
Disinfection byproducts
Sulfate radicals
In situ coagulation
Chlorination

ABSTRACT

Removal of natural organic matter (NOM) by conventional coagulation is often limited. This study investigated Fe(II)-activated sulfate-based oxidation systems (Fe(II)@SBOs), using peroxymonosulfate and peroxydisulfate (Fe(II)@PMS and Fe(II)@PS), for enhanced removal of NOM-derived disinfection by-products (DBPs). We provided fresh evidence exploring the synergistic roles of in situ radical oxidation and swift coagulation in Fe(II)@SBOs. At pH 7 and a low molar dose of DOC:Oxidant: Fe of 1:0.5:0.5, Fe(II)@PMS and Fe(II)@PS achieved better removals in DOC (55–59 %), fluorophoric substances (64–71 %), and DBP precursors (59–71 %), outperforming traditional Fe(III) by approximately 20–30 % for all tested parameters. At a high dose of 1:2:2, both Fe(II)@SBO systems reduced 80–90 % DBP precursors, which mitigated the calculated cytotoxicity potency of treated water by 0.5 to 1 order of magnitude lower than untreated water. Radical identification confirmed that Fe(II)@PMS generated $^{\bullet}OH$ and $SO_4^{\bullet-}$ radicals more effectively than Fe(II)@PS. These radicals oxidized NOM, transforming its carbon-carbon structure from a low (i.e. C—C/C—H, C—O) to a high degree of oxygenated carbonaceous groups (i.e. C═O, O—C═O). They reduced DBP formation via structural alternation of the precursor rather than complete organic mineralization, as evidenced by their minor impact in scavenging experiments. Instead, the newly formed Fe(III) characterized by monomeric and polymeric iron, governed the NOM removal process as demonstrated by chelating experiments. In situ Fe(III) facilitated swift coagulation for better charge neutralization with oxidized NOM and ultimately produced more compact flocs with a O—O structure. These characteristics were opposed to conventional Fe(III), which formed loose and elongated flocs. This study elaborates the synergistic roles of in situ oxidation and coagulation in Fe(II)@SBOs systems, offering promising alternatives to conventional coagulation for NOM-DBP mitigation.

1. Introduction

Natural organic matter (NOM) is a ubiquitous substance in surface water with source-dependent concentrations varying from several to over 20 mg C/L [1,2]. NOM consists of unsaturated C═C components with higher degrees of aromaticity and heteroatoms, such as nitrogen and sulfur [3,4]. It tends to be highly reactive with oxidants [5,6,7]. Consequently, NOM inevitably reacts with chlorine during pre- and post-chlorination processes to produce undesirable chlorinated disinfection by-products (DBPs) [5,8]. Nowadays, >700 DBP compounds have been identified [9,10,11]. Some regulated DBPs (i.e. trihalomethanes (THMs), haloacetic acids (HAAs)) can be found at elevated levels 1000 times higher than those of emerging contaminants i.e. pharmaceuticals or poly-fluoroalkyl substances [10,12]. Due to the intrinsic carcinogenicity of chlorinated DBP compounds [13,14], DBP formation has become a major public health concern in the global drinking water supply [11].

Conventional iron-based coagulation can remove 16–76 % of NOM precursors, with removal efficiencies varying widely depending on the water source and treatment conditions (**Table S1**) [15,16,17,18]. These conventional methods could also moderately remove dissolved organic nitrogen (DON removal of 41–47 %). However, they may require extremely high coagulant doses, i.e. 40 mg/L poly aluminum chloride or 70 mg/L ferric chloride [19]. Enhanced coagulation using hybrid organic silicate iron coagulants can somewhat achieve higher NOM removal rates, up to 90 % [18]. However, the 20–90 % reduction of

* Corresponding author.
E-mail address: huang@nctu.edu.tw (C. Huang).

https://doi.org/10.1016/j.seppur.2025.135378
Received 16 August 2025; Received in revised form 17 September 2025; Accepted 25 September 2025
Available online 29 September 2025
1383-5866/© 2025 Elsevier B.V. All rights are reserved, including those for text and data mining, AI training, and similar technologies.

NOM precursor is not always equally effective for DBP minimization due to the complex reactivity of residual NOM with chlorine. Even when conventional coagulation reduces a large quantity of NOM, some small molecular fractions remaining after treatment can still lead to unexpected DBP formation during subsequent chlorination processes.

The limitations of conventional coagulation in removing NOM precursors are increasingly evident, which highlights a pressing need to explore more robust alternatives. In this context, Fe(II)-activated sulfate-based oxidation-coagulation processes (Fe(II)@SBOCs), including peroxymonosulfate (Fe(II)@PMS) and persulfate (Fe(II)@PS) are highly promising. The Fe(II)@SBOCs systems leverage synergistic benefits from in situ radical oxidation and swift coagulation in a single process [15,20,21,22]. First, these benefits are attributed to their capabilities to generate potent oxidative radicals, primarily sulfate ($SO_4^{\bullet-}$, $E_0 = 2.5–3.1$ V) and hydroxyl radicals ($^{\bullet}OH$, $E_0 = 1.8–2.7$ V), through the homolytic cleavage of O—O bonds of PMS or PS [23,24,25]. Both radicals exhibit highly reactive and non-selective oxidation to break down electron-rich organic molecules that are recalcitrant to conventional coagulation alone [26,24,27]. Second, the Fe(II)@SBOC processes incorporate swift coagulation via the oxidation of Fe(II) to Fe(III), which rapidly forms in situ iron hydroxide colloids [15,22]. The in situ Fe(III) functions as more effective coagulants in removing both oxidized organic matter and particulate contaminants [21].

In this study, the dual-function mechanism of Fe(II)@SBOCs was hypothesized to provide a more integrated approach for effectively addressing the limitations of traditional coagulation methods. Here, we systematically addressed critical knowledge gaps in understanding the synergistic interplay between $SO_4^{\bullet-}$ radical-driven oxidation and dynamic in situ coagulation processes, which have remained largely unexplored in existing literature. General coagulation involves the reduction of repulsive potential within a colloidal double layer, which is promoted by hydrolyzed metal species [28]. We speculated that the in situ produced Fe(III) colloids would surpass conventional preformed Fe-based coagulants because of their ability to complex and cross-link with NOM via the magnetic crystal Fe_3O_4 nanoparticles or various positively charged iron oxyhydroxides [15,29,22]. Pan et al. [30] found that as the carboxylic group content increases, NOM is more readily removed by metal coagulants. This may be attributed to the ligand-to-metal charge transfer reactions between carboxylic groups and metal hydroxides [28,31], forming carboxylate-metal bonds, such as Fe-O-C.

The first objective of this study was to evaluate the removal of NOM precursor by Fe(II)@PMS and Fe(II)@PS and its corresponding impact on NOM-derived DBP mitigation. The second objective aimed to elucidate two key mechanisms in these novel hybrid systems, including (i) the role of in situ radical oxidation and (ii) the roles and dynamics of in situ coagulation/flocculation. Through this study, we aim to contribute valuable and insightful understanding into the innovative Fe(II)@SBOCs processes for NOM-DBP mitigation, potentially advancing the practices of sustainable water treatment for safe drinking water practices.

2. Materials and methods

2.1. Materials

All chemical reagents utilized in this study were of ACS grade and were used without further purification unless otherwise stated. Deionized water (DI, 18.2 MΩ.cm, Arium®mini Göttingen, Germany) was employed for all reagent preparations. Potassium peroxymonosulfate (100 %, Sigma-Aldrich) and sodium persulfate (99 %, Sigma-Aldrich) were employed as oxidants. $FeCl_3$ (98 %, Alfa Aesar) and $FeSO_4$ (100 %, JT beaker) were utilized for preparing stock Fe(III) and Fe(II) solutions (at 2000 mg/L), which were subsequently added to the raw water to achieve the desired concentrations. Sodium nitrite (99.5 %, Sigma-Aldrich) and potassium iodide (100 %, Sigma-Aldrich) were employed as scavengers of reactive oxygen species (ROS). 5,5-dimethyl-1-pyrroline N-oxide (98 %, Sigma-Aldrich) was used as spin-trapping reagents for Electron Paramagnetic Resonance (EPR) analysis. Potassium iodide (100 %), sodium nitrite (100 %), sodium sulfate (99 %), sodium pyrophosphate (99 %), and methyl tert-butyl ether (MtBE, 98 %) were obtained from Sigma-Aldrich. For the chlorination experiment, a chlorine stock solution was prepared from 5 % sodium hypochlorite purchased from JT Baker.

All experiments were conducted with the natural raw water collected from the source of the Hsinchu Water Purification Plant, Taiwan. **Table S2** gives the characteristics of the natural raw water. Note that the raw water source was characterized as having low organic and metal ion contents (with DOC <1.2 mg/L). NOM from the International Humic Substances Society (IHSS), specifically Suwannee River NOM (2R101N), was added to the raw water until the desired dissolved organic carbon (DOC) concentration at approximately 4–5 mg/L, a concentration commonly found in natural waters worldwide.

2.2. Jar-test experiment for Fe(II)@SBOC processes

All chemical dosing with Fe(III) for conventional coagulation and with Fe(II)@PMS/PS for hybrid oxidation-coagulation was carried out in a Phipps & Bird programmable jar tester (Model PB900) using a 500 mL beaker. Fe(III), Fe(II), or PMS/PS reagents were added directly to the solution within 1 min of rapid mixing at 200 rpm, followed by slow mixing at 30 rpm for 20 min, and then settling for 10 min. Meanwhile, the solution pH was adjusted with 1 M NaOH and 1 M H_2SO_4. After settling, the supernatants from the Fe(II)@SBOC processes were filtered through 0.45 μm before further water quality analyses.

The NOM removal of Fe(II)@SBOC processes was investigated under varying pH values of 7, 8, and 9 and chemical dose with [DOC]:[Oxi]:[Fe] molar ratios of 1:0.5:0.5, 1:1:1, and 1:2:2. In particular, the pH 7–9 range were compared to represent the common operating range for drinking water treatment and allowed us to explore the unique advantages of simultaneous radical oxidation and in-situ coagulation under practical conditions where conventional coagulation is less efficient. The [Oxi]:[Fe(II)] ratio of 1:1 was identified as the optimal activation ratio, as it likely results in negligible chemical residuals after treatment, based on our previous study [15]. The designed doses for oxidant and Fe were based on the proportional molar concentration respective to DOC concentration expressed as carbon in μM. For example, given DOC = 4.3 mg/L equivalent to 360 μM as carbon, the doses of Fe(II) and oxidants at [DOC]:[Oxi]:[Fe] ratio of 1:1:1 were 360 μM each. Optimal pH and dose were accordingly determined using the reductions of DOC and EEM. Furthermore, the DBP formation potential test was conducted on treated water samples under optimal dosing conditions of Fe(II)@PMS and Fe(II)@PS. The chlorination was carried out with excess chlorine added to maintain a residual level of approximately 0.5–1 mg/L after 24 h. Afterward, the chlorinated samples were subjected to liquid-liquid extraction using MtBE saturated with Na_2SO_4 prior to the DBP analysis.

2.3. Characterization of water matrix

All water quality characterizations were carried out in triplicate. DOC analysis was measured by a TOC analyzer (Shimadzu, TOC-5000 A, Japan) connected with an ASI-L automatic suction device, with an operating pressure higher than 3 kg/cm^2. All samples were filtered through a 0.45 μm membrane, then added 2–3 drops of HCl (1,1 *V*/V) for acidification to pH <2 before DOC measurement. The pH of water samples was determined by a pH meter (sensIONTM+, HACH, USA). The Zeta potential of the supernatants was measured using a Malvern ZetaSizer Nano ZS90 (Malvern, UK). The fluorescent organic components in the water were analyzed using a Cary Eclipse fluorescence excitation-emission matrix (EEM) spectrophotometer (Agilent Technologies, USA). Detailed EEM setup followed our previous study [32]. Briefly, all samples were subject to 0.45 μm filtration and diluted by DI water to obtain a UV absorbance <0.1 to avoid the inner filter effect before EEM scanning if needed. The scanning ranges of excitation/

emission (ex/em) were 200–400 nm and 250–550 nm, respectively, with a scan rate of 10 nm and 2 nm increments. The average fluorescent intensity (AFI) was calculated based on the 3D EEM contour plot after subtracting for the blank, as well as Rayleigh and Raman scattering interferences. Briefly, AFI of each component was calculated by dividing the mean fluorescence signal within each defined spectral region to the total number of data points in that region.

2.4. Oxidant concentration and radical identification

PMS and PS concentrations were determined using a colorimetric KI/$NaHCO_3$ method adapted from Liang et al. [33]. This method relies on the reactions of PMS/PS with iodide in the presence of sodium bicarbonate, forming a yellow iodine complex that can be quantitatively measured. Briefly, the KI/$NaHCO_3$ reagent was freshly prepared by adding 4 g KI and 0.2 g $NaHCO_3$ to 40 mL DI water. The calibration curve was prepared at the oxidant concentrations of 0–200 μM (**Fig. S1**). Before the measurements, 0.1 mL of the water sample was mixed with 40 mL of the KI/$NaHCO_3$ reagent. The mixture was hand-shaken and allowed to equilibrate for 15 min. The absorption spectrum was acquired using a spectrophotometer (UH 5300, Hitachi, Japan) at a wavelength of 288 nm.

To investigate the roles of in situ radical oxidation, the in-situ formation of hydroxide and sulfate radicals was detected using an EPR spectrometer (Bruker ELEXSYS-E580, Germany) by adding DMPO reagents for trapping DMPO-$OH^{\bullet}$ and DMPO-$SO_4^{\bullet}$ adducts. We mainly focused on $OH^{\bullet}$ and $SO4^{\bullet-}$ radicals, as they are well established as the primary oxidants in Fe(II)-activated PS and PMS systems for NOM degradation [34,35]. Available literature consistently reports that the oxidation capacity and reaction rates of $OH^{\bullet}$ and $SO4^{\bullet-}$ radicals are 2–4 orders higher than superoxide-related species [35,36]. Furthermore, radical scavenging tests were conducted to confirm the participation of $^{\bullet}OH$ and $SO_4^{\bullet-}$ radicals [20]. To further confirm the roles of radicals, both $NaNO_2$ and KI were used to cross-check the participation of $^{\bullet}OH$ and $SO_4^{\bullet-}$ radicals in the systems. The radical scavenging experiments were conducted under the same jar test apparatus.

2.5. Iron speciation and coagulation dynamics

The concentration of soluble iron was measured using an inductively coupled plasma optical emission spectrometry (Agilent, 710 Series ICP-OES, USA). Speciation of the in situ produced Fe(III) species can be categorized into Fe_a, Fe_b, and Fe_c, representing monomeric, oligomeric or small polymeric, and colloidal unreactive Fe(III), respectively [37,38,39]. These species react differently with ferron (8-hydroxy-7-iodo-5-quinoline-sulfonic acid) reagent: Fe_a reacts rapidly within 1 min, Fe_b reacts more slowly over 180 min, and Fe_c does not react within the measurement period [40]. The resulting colored complexes can be measured spectrophotometrically at 600 nm. In detail, the ferron working solution consisted of three reagents. Reagent A (0.2 % ferron) was prepared by dissolving 0.5 g of ferron in distilled water. This reagent was boiled to remove dissolved CO_2 and filtered through a 0.45 μm filter prior to use. Reagent B (20 % *w/v* NaAc) was made by dissolving 50 g of sodium acetate anhydrous in 250 mL of distilled water. Reagent C (1,1 *v*/v HCl) was prepared by mixing 250 mL of 37 % HCl (Sigma-Aldrich) with 250 mL of distilled water. These reagents were mixed in a specific volumetric ratio (A:B:C = 5:4:2 mL), with reagents B and C combined first, followed by reagent A. An aliquot of 10 mL water sample was added to the reagent mixture in a centrifuge tube and quickly diluted to 50 mL. After vertexing, the ferron sample was measured for absorbance at 600 nm in 1 min and 180 min, assigned for the levels of Fe_a and Fe_b, respectively. Their concentrations were calculated using the calibration curve made from the 1000 mg/L total iron standard for atomic absorption spectrometry (**Fig. S2**). The level of Fe_c (non-reactive Fe) was obtained by subtracting the sum of Fe_a and Fe_b from the total Fe.

The coagulation dynamic of Fe(II)@SBOC systems was monitored using a portable visualizing technique FlowCAM (Fluid Imaging Technologies, US). The experimental methodology for FlowCAM was adapted from our prior work with minor modifications [41,29]. A comparison of the precipitates was made after rapid mixing (1 min) and slow mixing (20 min) for Fe(III) only, Fe(II)@PMS, and Fe(II)@PS. FlowCAM was equipped with a 4× magnification objective and a 0.3 mm flow cell. A 20 mL sample was introduced into the flow cell by a 5 mL programmable syringe pump at a flow rate of 1 mL/min for 1 min (**Fig. S3**). The auto image mode was triggered to capture particle size ranging from 10 to 500 μm at 20 frames per second. Particle concentration and morphological properties were computationally calculated in VisualSpreadsheet.

2.6. Chemical functional compositions of precipitates

To gain deeper insights into the chemical compositions and functional groups of the precipitates post-treatments, an X-ray photoelectron spectroscopy (XPS, PHI Quantera II, ULVAC-PHI, Japan) was applied for full-scan (0–1400 eV) and high-resolution scans for C1s (300–275 eV), O1s (545–520 eV), and (Fe2p (740–700 eV) elements. The XPS survey utilized an Al Kα X-ray source with an energy of 1486.6 eV. All experimental setups of XPS followed our previous study [20]. Prior to analysis, precipitate samples after rapid and slow mixing were collected using a 0.45 μm membrane filter and subsequently freeze-dried. For data quantification, the XPS spectra were deconvoluted using Peakfit software (Systat, Software Inc., USA), as described elsewhere [42].

2.7. Chlorination experiments and DBP analysis

Before chlorination for the DBP formation test, the appropriate chlorine dose was determined by pre-tests to ensure a 0.5–1.0 ± 0.4 mg/L residual after 24 h in a dark incubation at room temperature. Treated water samples were placed in headspace-free 43.5 mL amber bottles sealed with a Teflon-faced cover and subjected to 24 h chlorination at room temperature in the dark. After 24 h, the chlorine residue was quenched by 0.1 mL of 30 g/L ascorbic acid before subsequent DBP extraction.

The extraction method was adopted from US EPA method 551.1 with slight modification followed elsewhere [43]. 30 mL of samples were saturated with 12 g of baked Na_2SO_4 and 3 mL MtBE with 1,2,3-Trichloropropane as an internal standard, and shaken vigorously for 2 min. The extract was analyzed by a gas chromatography-electron-capture detector (GC-ECD, Thermo Scientific™/ micro ECD) equipped with a DB-1701 column (30 m × 0.25 mm ID, 0.25 μm film thickness). The analyzed disinfection by-products (DBPs) included trichloromethane (TCM), trichloroacetonitrile (TCAN), dichloroacetonitrile (DCAN), trichloronitromethane (TCNM), dichloropropanone (DCP), and trichloropropanone (TCP). All DBP measurements were carried out in duplicate.

3. Results and discussion

3.1. Mitigation of NOM precursor by Fe(II)@SBOCs

Fig. 1 shows the removal of NOM precursor by Fe(II)@SBOCs as functions of pH and chemical dose. At the dose of [DOC]:[Fe] of 1:0.5 and pH 7, conventional Fe(III) coagulants exhibited limited NOM removal, accounting for 20–32 % (Fig. 1A). Note that the NOM removal was also minimal for all control groups, i.e. 23–30 % for oxidant-alone PMS and PS and <20 % for Fe(II)-alone (**Fig. S4**). Both Fe(II)@PMS and Fe(II)@PS achieved the highest DOC removal rates of 55–59 %, representing a substantial improvement of approximately 30 %. Increasing the solution pH to 8 and 9 decreased the removal efficiencies by 8 % and 25 % for Fe(II)@PMS and Fe(II)@PS, respectively (Fig. 1A). Apparently, Fe(II)@PMS was less impacted by the pH increase compared to Fe(II)@PS, attributed to two key factors related to Fe(II) accessibility

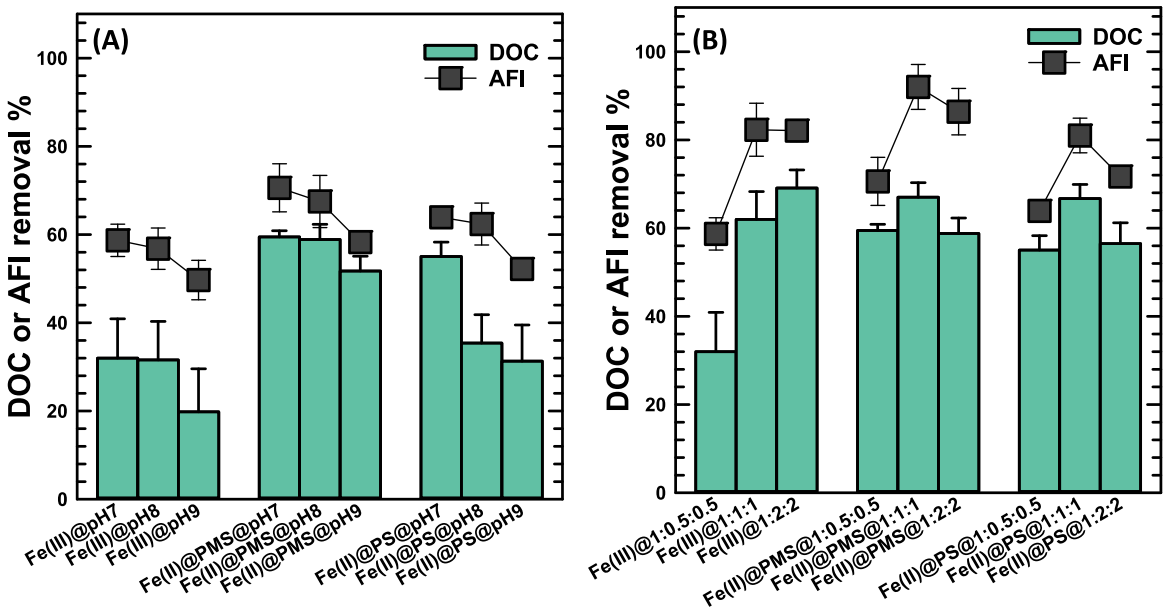

Fig. 1. Removals of DOC and fluorophoric substances as functions of **(A)** pH and **(B)** chemical dose for Fe(III), Fe(II)@PMS, and Fe(II)@PS. The AFI of each component was calculated by dividing the mean fluorescence signal within each defined spectral region to the total number of data points in that region. Experimental conditions: $[DOC]_0$ = 4–5 mg/L; **(A)** The experiments were conducted at a fixed [DOC]:[Oxi]:[Fe] of 1:0.5:0.5 under varying pH 7, 8, and 9; **(B)** The experiments were conducted at pH 7 under varying [DOC]:[Oxi]:[Fe] ratios of 1:0.5:0.5, 1:1:1, and 1:2:2.

and oxidant activation. First, Fe(II) precipitation at alkaline pH conditions reduced the available Fe(II) for activation [25]. This precipitation rendered Fe(II) less accessible to both oxidants, though with differential impacts. Second, the symmetric structure of PS made it less ready for activation by the diminishing Fe(II) [26,44]. By contrast, the asymmetric structure of PMS allowed for more efficient activation by iron hydroxide as an electron acceptor despite its higher O—O bond dissociation energy than PS [25,35,45]. This structural advantage enabled PMS to better utilize the limited accessible Fe(II) under challenging pH conditions.

Fig. 1B illustrates the DOC removal efficiencies at varying molar ratios of 1:0.5:0.5, 1:1:1, and 1:2:2. The ratio of PMS/PS versus Fe(II) was maintained at a fixed 1:1 ratio to ensure efficient activation and minimize the remaining reagents [15]. Both Fe(II)@PMS and Fe(II)@PS systems achieved optimal removal efficiencies at a 1:1:1 M ratio, accounting for 67 % and 66 %, respectively. These removal rates were slightly higher than conventional Fe(III) of 62 % at the same molar dose. Further increasing the dose insignificantly improved the removal rates. The limited improvement at the higher dose of 1:2:2 likely resulted from radical scavenging effects and competing side reactions [25], where excess oxidant and Fe(II) could intercept generated reactive species or engage in reactions that did not contribute to DOC removal. Compared to previous studies (as summarized in **Table S1**), the DOC removal for conventional Fe(III) and Fe(II)@SBOs significantly varied based on the conditions and research methodologies, with 17–76 % for Fe(III), 16–43 % for Fe(II)@PMS, and 13–79 % for Fe(II)@PS [34,46,47,48]. Our study presented that Fe(II)@PMS and Fe(II)@PS provided relatively better DOC removal efficiencies compared to ferric chloride across all doses, aligning with the higher end of the removal ranges observed in previous studies (rates around 59–67 % for PMS and 55–67 % for PS).

Furthermore, fluorophoric substances of NOM were significantly reduced after treatments relative to raw water (**Fig. S5**). The reduction of total AFI (as shown in **Figs. 1A** and **B**) presented similar trends to DOC removal. At pH 7, the reduction of EEM intensities was highest at the [DOC]:[Oxi]:[Fe] of 1:1:1 for both Fe(II)@PMS and Fe(II)@PS, accounting for 92 % and 82 % intensity reductions, respectively (Fig. 1C). These results suggested the order of removal effectiveness in DOC and fluorophoric substances followed: Fe(II)@PMS > Fe(II)@PS ~ Fe(III). Note that across all experimental conditions, residual oxidants and residual irons after Fe(II)@SBOs and Fe(III) were mostly minimal to nondetectable (**Table S3**), indicating complete consumption of reagents and negligible interference with subsequent experiments. The dosing condition at [DOC]:[Oxi]:[Fe] of 1:1:1 and pH 7 was thus selected for subsequent experiments.

3.2. Mitigation of DBPs by Fe(II)@SBOC systems

To further validate the efficacy of Fe(II)@SBOC systems in DBP (i.e. TCM, TCAN, DCAN, TCNM, DCP, and TCP) mitigation, the formation potential test was applied for the raw and treated water samples after Fe(III), Fe(II)@PMS, and Fe(II)@PS (Fig. 2). Raw water yielded the highest concentrations of DBPs across all measured species, with elevated levels of TCM (136 μg/L), TCNM (27.2 μg/L), and DCAN (20.4 μg/L) (Fig. 2A). At a low dose of 1:0.5:0.5, conventional Fe(III) coagulation moderately reduced ~55 % total DBP formation, contributed by TCM, TCNM, and DCP reduction. Increasing the Fe(III) dose to 1:2:2 further improved the overall DBP mitigation to 77 %. By contrast, both Fe(II)@PMS and Fe(II)@PS treatments displayed better DBP mitigation. These methods reduced 59–71 % of total DBP precursor at 1:0.5:0.5 and achieved near-complete removal ~90 % at 1:2:2, indicating their superiority in DBP precursor mitigation compared to conventional Fe(III) coagulation.

The calculated cytotoxicity index (CCI) is often used to compare the toxicity of treated water upon chlorination [15,49]. Fig. 2B shows the CCI determined by using the LC_{50}-weighted concentrations of DBPs, which is a good indication for DBP-associated cytotoxicity of different treated waters. This index reflects the concentration required in the original water sample to achieve a 50 % decrease in the density of Chinese hamster ovary (CHO) cells [50]. The LC_{50} values of each DBP were collected from previous publications [51,49], as given in **Table S4**. Unfortunately, the CCI value of DCP was excluded from CCI assessment due to the unavailability of their CHO cytotoxicity data in the current literature database. Though this exclusion might limit our complete toxicological evaluation, the CCI values derived from the remaining characterized DBPs still provided valuable insights into the relative treatment comparison.

Both treated water after Fe(II)@PMS and Fe(II)@PS significantly

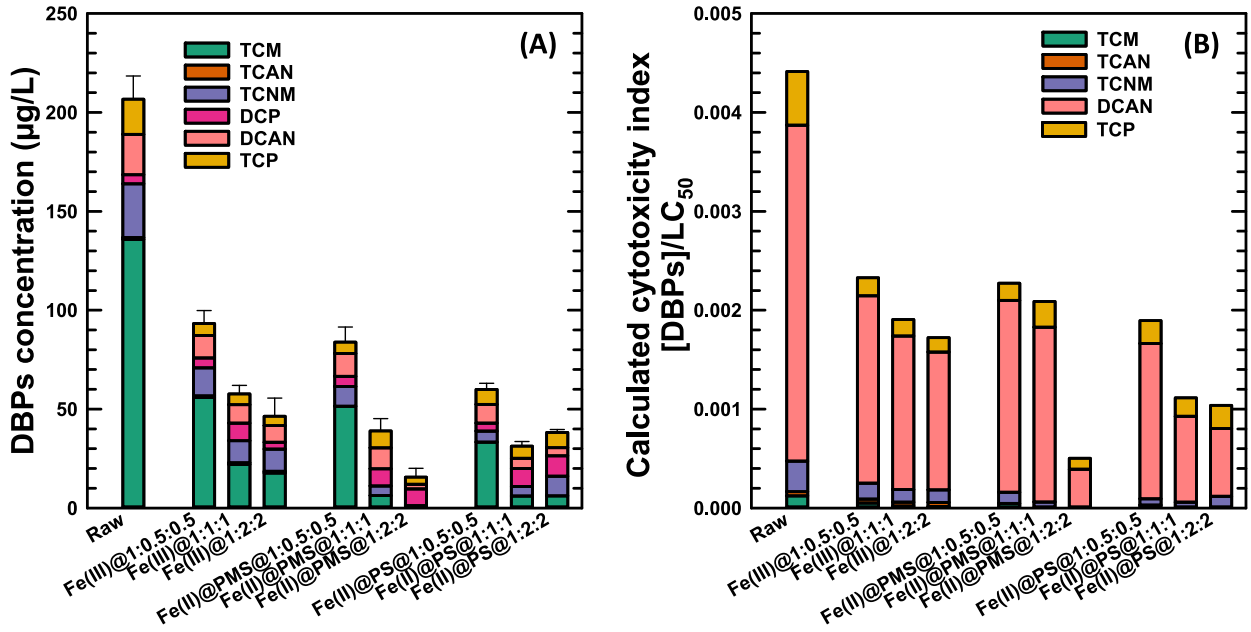

Fig. 2. **(A)** DBP formation and **(B)** the calculated cytotoxicity index in chlorinated water after Fe(III), Fe(II)@PMS, and Fe(II)@PS processes. The experiments were conducted at pH 7 under [DOC]:[Oxi]:[Fe] variations of 1:0.5:0.5, 1:1:1, and 1:2:2 and $[DOC]_0$ = 4–5 mg/L.

lowered CCI values compared to the raw water and the treated water with conventional Fe(III) (Fig. 2B). Their reductions were approximately 0.5 to 1 order of magnitude lower than those of raw water at the sufficient dosing of 1:2:2 conditions. This superior performance was attributed to the generation of highly reactive radicals, including sulfate radicals ($OH^{\bullet}$ and $SO_4^{\bullet-}$) facilitated during PMS and PS activation. These radicals effectively mineralized NOM precursors, altering their carbonaceous functional structures through enhanced oxidation processes. Additionally, Fe(II) was oxidized to Fe(III), which acted as a coagulant to adsorb small molecular substances, promoting swift coagulation mechanisms that further reduced DBP precursors. These synergistic effects of radical generation and in situ coagulation highlight the efficacy of Fe (II)-activated systems in mitigating DBP precursors. Their prominent roles will be elaborated and discussed in detail in the later section.

3.3. Roles of in situ radical oxidation in Fe(II)@SBOCs

The generation of free radicals in Fe(II)@SBOC processes was clarified using EPR coupled with DMPO trapping agents. Figs. 3A and B depict the 1:2:2:1 and 1:1:1:1:1:1 signals of DMPO-$OH^{\bullet}$ and DMPO-$SO_4^{\bullet-}$ adducts, indicating the formation of $OH^{\bullet}$ and $SO_4^{\bullet-}$ radicals in both systems [52,26,48]. At the same molar basis, Fe(II)@PMS appeared to produce both DMPO-$OH^{\bullet}$ and DMPO-$SO_4^{\bullet-}$ more intensively than Fe(II) @PS, suggesting its more robust capacity in radical generation. The advancement of Fe(II)@PMS could be attributed to the activation mechanisms of PMS, which is more efficient than PS [35,25]. In particular, activation of PMS and PS by Fe(II) begins with the heterolytic (electron transfer) cleavage of the O—O bond in HSO_5^- and $S_2O_8^{2-}$ [24]. While PS initially generates only $SO_4^{\bullet-}$ radicals, PMS produces both $OH^{\bullet}$ and $SO_4^{\bullet-}$ radicals [26,27]. The sulfate radicals then react with hydroxide ions to form hydroxyl radicals ($OH^{\bullet}$) [35]. The multi-step process in PS activation, coupled with its structural limitations, likely resulted in less intensive production of both DMPO-$OH^{\bullet}$ and DMPO-$SO_4^{\bullet-}$ adducts compared to the Fe(II)@PMS system.

Subsequently, the participation of $OH^{\bullet}$ and $SO_4^{\bullet-}$ radicals in NOM reduction was corroborated using scavenger experiments with KI and

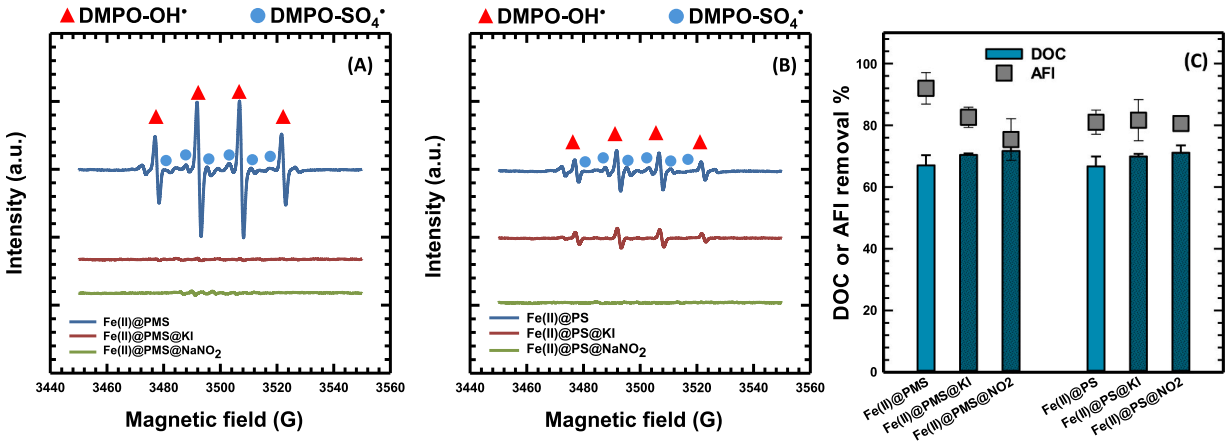

Fig. 3. Radical formation in **(A)** Fe(II)@PMS and **(B)** Fe(II)@PS with and without additions of KI and $NaNO_2$ scavengers as observed by EPR spectra after 1 min of rapid mixing. **(C)** Impacts of KI and $NaNO_2$ additions on the removal of DOC and fluorophoric substances in Fe(II)@PMS and Fe(II)@PS. Both EPR scanning and scavenging experiments were conducted at pH 7 under [DOC]:[Oxi]:[Fe] = 1:1:1. Experimental conditions: $[DOC]_0$ = 4–5 mg/L; [DMPO] = 11 mM, [KI] = [$NaNO_2$] = 1.8 mM.

$NaNO_2$ additions with rate constants of $k_{OH^\bullet,I^-} = 1.0 \times 10^{10}$, $k_{SO_4^{\bullet-},I^-} = 3.8 \times 10^9$, $k_{OH^\bullet,NO_2^-} = 6.0 \times 10^{10}$, and $k_{SO_4^{\bullet-},NO_2^-} = 8.8 \times 10^8$ M^{-1} s^{-1}, respectively [53,54]. The additions of two radical scavengers diminished EPR signals, confirming $OH^\bullet$ and $SO_4^{\bullet-}$ deletions in the tested solutions for both Fe(II)@PMS and Fe(II)@PS systems (Figs. 3A and B). However, the scavenger-added groups (KI and $NaNO_2$) showed nominal deviations compared to the control, accounting for less than ±2 % DOC and ± 8 % EEM removal variations in the two systems. These results suggested that $OH^\bullet$ and $SO_4^{\bullet-}$ free radicals played a limited role in the overall removal of NOM in Fe(II)@SBO systems.

3.4. Roles and dynamics of in situ coagulation in Fe(II)@SBOCs

The roles of in situ coagulation in Fe(II)@SBOC system were elaborated using pyrophosphate (NaPP), an inert chelating reagent that complexes with Fe species and barely reacts with $OH^\bullet$ and $SO_4^{\bullet-}$ radicals [44,55]. When introduced into the tested solutions, NaPP stabilizes Fe (II) and terminates the formation of in situ Fe(III), thus impeding the coagulation process. Upon the addition of NaPP at 1.8 mM, residual levels of soluble Fe ions remained over 90 % (Fig. 4A), and no visible flocs could be formed. The termination of in situ coagulation significantly decreased the DOC removal efficiency, notably with a 61 % reduction relative to the control for Fe(II)@PMS, followed by approximately 53 % reduction for Fe(II)@PS. The result indicated that DOC removal in Fe(II)@SBOC systems was primarily facilitated by in situ coagulation. However, the interruption of Fe(III) coagulation did not fully inhibit fluorophoric component mitigation. Despite coagulation termination, all experimental groups-maintained removal efficiencies of over 80 % for total AFI. This persistent removal suggested that residual oxidative radicals may contribute to fluorophoric substance reduction even when coagulation is disrupted.

Given that in situ Fe(III) are hydrolyzed species, they distinctively react with ferron to form complexes, categorizing into monomers (Fe_a), oligomers (Fe_b), and highly polymerized colloidal species (Fe_c) [38,39].

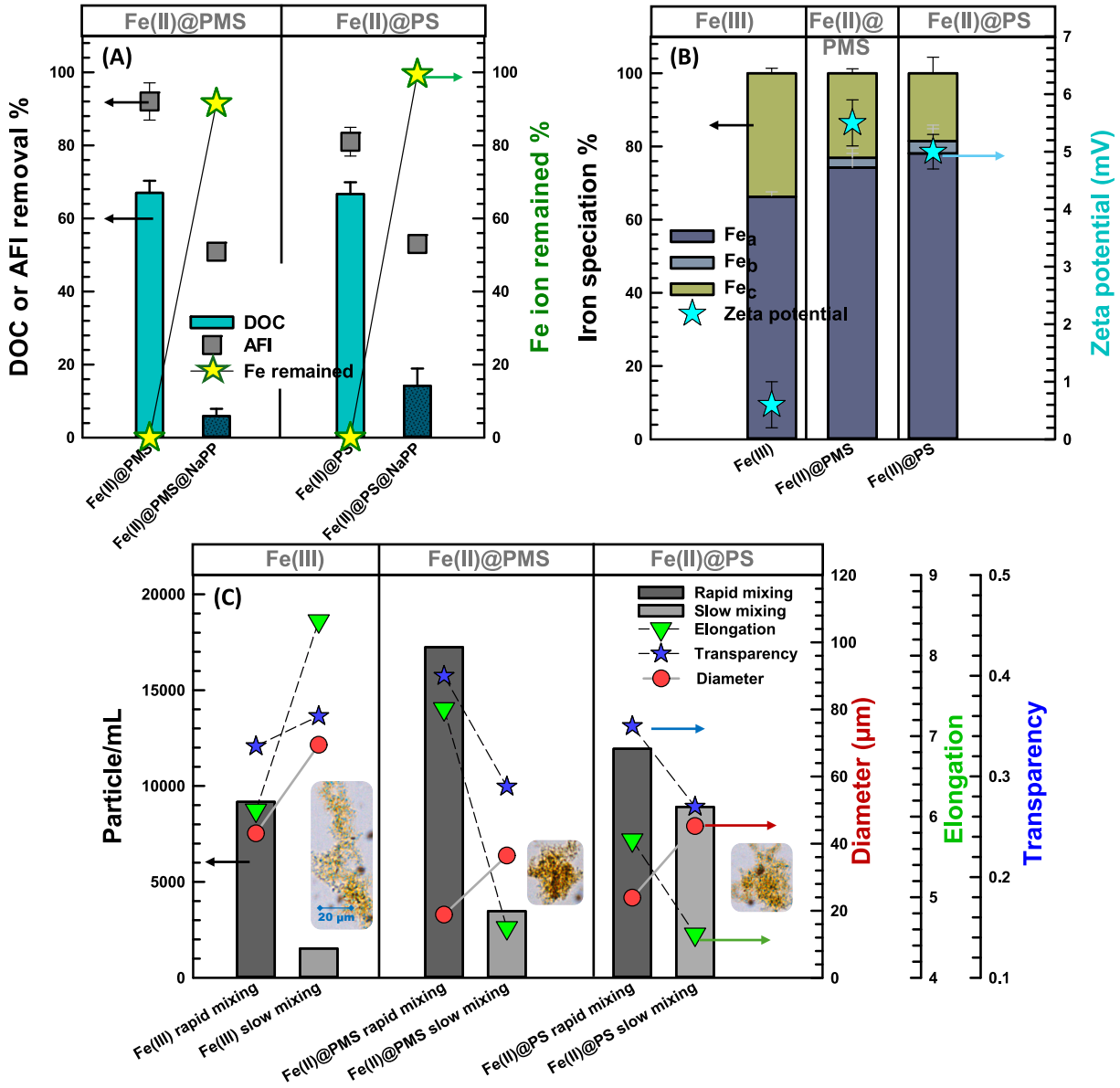

Fig. 4. **(A)** Impacts of sodium pyrophosphate additions on the removal of DOC and fluorophoric substances and remaining soluble Fe in Fe(II)@PMS and Fe(II)@PS. **(B)** Distribution of iron species and the corresponding zeta potential for Fe(III), Fe(II)@PMS, and Fe(II)@PS. **(C)** Flocculation dynamics after rapid and slow mixing for Fe(III), Fe(II)@PMS, and Fe(II)@PS, with inset microscopic images representing precipitated flocs after slow mixing. Experiments were conducted at pH 7 with a ratio of [DOC]:[Oxi]:[Fe] = 1:1:1, $[DOC]_0$ = 4–5 mg/L, and [NaPP] = 1.8 mM.

Comparison was made between conventional Fe(III) coagulation and Fe(II)@SBOCs to differentiate their hydrolyzed iron speciation (Fig. 4B). In particular, preformed Fe(III) primarily produced 66 % Fe_a species and 33 % Fe_c, with minimal Fe_b observed. Fe(II)@PMS and Fe(II)@PS generated 75–78 % Fe_a, 18–23 % Fe_c, and again minimal 2–3 % Fe_b detected. In general, Fe_a represents the hydroxylated iron monomeric species (i.e. $[Fe(H_2O)_6]^{3+}$, $[Fe(H_2O)_5(OH)]^{2+}$, or $[Fe(H_2O)_4(OH)_2]^{+}$, while Fe_b refers to those oligomeric species carrying more positively charged iron units, such as $[Fe_2(OH)_2]^{4+}$, $[Fe_3(OH)_4]^{5+}$ or $[Fe_4(OH)_6]^{6+}$ [40,56]. These oligomers are formed through the condensation of monomeric species and exhibit intermediate reactivity and stability with ferron reagent compared to monomers and highly polymerized colloidal species (Fe_c) [40]. Both Fe_a and Fe_b are positively-charged hydroxylated species [37,38], which have a high tendency to neutralize the negatively-charged carboxylic groups of NOM, consequently promoting the enhanced formation of micro-flocs [28]. Indeed, better improvement of charge neutralization of the resulting suspensions became more apparent after Fe(II)@PMS and Fe(II)@PS processes compared to Fe(III) coagulation, exhibited the highest surface charge with a zeta potential of beyond 5 mV (Fig. 4B). The sequence of observed potentials after treatment was Fe(II)@PMS > Fe(II)@PS > Fe(III). These results suggested that in situ coagulation in Fe(II)@SBOC systems originated from the hydroxylated monomeric and oligomeric Fe(III) species, which featured a more positively charged surface, indicating an enhanced charge neutralization capability.

Furthermore, this study employed the imaging tool FlowCam to observe the dynamics of micro-floc aggregation and their resulting morphology during 20 min of flocculation (Fig. 4C). The representative images of the resulting micro-flocs after rapid and slow mixing from the three processes are given in **Fig. S6**. All yielded flocs showed typical brown-yellowish and appeared in an amorphous structure, aligning with previous studies [21,37,38]. Fe(III) tended to form larger and less uniform flocs, while Fe(II)@PMS and Fe(II)@PS resulted in smaller and more regularly shaped flocs. After 1 min of rapid mixing, Fe(II)@PMS produced flocs with the highest particle concentration (17,000 particles/mL) and the smallest size (20 μm). Fe(II)@PS resulted in slightly larger flocs (24 μm) with a concentration of 12,000 particles/mL. In contrast, Fe(III) formed the largest flocs (43 μm) but with the lowest concentration (~9000 particles/mL). After slow mixing, floc aggregation was evident as particle numbers decreased and diameters increased across all groups. Dynamic aggregation was most efficient in Fe(II)@PMS with ~80 % reduction in particle number, followed by Fe(III) and Fe(II)@PS. Moreover, particle sizes increased by a factor of 1.9 for Fe(II)@PMS > 1.8 for Fe(II)@PS > 1.6 for Fe(III).

From the geometrical properties, Fe(III) formed flocs with an elongated, amorphous shape that was neither densely arranged nor compact (Fig. 4C). By contrast, Fe(II)@PMS and Fe(II)@PS similarly produced more compact, dense, and stronger flocs. Two geometrical properties of flocs were characterized including elongation (EnI) and transparency indexes (TrI). EnI quantifies the deviation of a particle from a circular shape, calculated as the ratio of its major to minor axis, starting at 1 for circular particles and increasing with elongation. TrI evaluates the light transmission ability of a particle, ranging from 0 for completely opaque to 1 for completely transparent particles. They both directly reflect the compactness of the flocs; The less elongated and less transparent characteristics of a particle indicate higher structural density and compactness. As shown in Fig. 4C, both EnI (6.1 to 8.4) and TrI (0.33 to 0.36) of Fe(III) flocs increased during flocculation. However, both indices consistently decreased in Fe(II)@PMS and Fe(II)@PS, with EnI dropping from 7.4 to 4.6 and 5.7 to 4.5 and TrI decreasing from 0.40 to 0.29 and 0.35 to 0.27, respectively. These results indicated that the shape of conventional Fe(III) flocs became more elongated with a loose structure after flocculation. In contrast, Fe(II)@SBOC yielded in situ Fe(III) flocs that exhibited an opposite trend, becoming more circular and compact.

3.5. Formation of iron-enriched oxygenated precipitates in Fe(II)@SBOCs

Conventional Fe(III) and in situ Fe(III) displayed profound distinctions in iron speciation and coagulation/flocculation dynamics. This study further examined the compositional differences among their coagulated precipitates using XPS to elucidate the underlying mechanisms (Fig. 5). Without any treatment, the pristine NOM sample was constituted mainly of 65 % C and 34 % O with less than 1 % Fe, indicating its organic nature (Fig. 5A). After 1 min of rapid mixing, all precipitates were mineralized, with their C contents reduced to 40 % for Fe(III) and 30–35 % for Fe(II)@SBOC treatments. All coagulated precipitates were incorporated by iron oxides, where O and Fe contents increased to 50–54 % and 10–16 %, respectively. Compared to Fe(III), Fe(II)@PMS and Fe(II)@PS produced more apparent iron-enriched oxygenated products, indicating a distinct incorporation of iron and oxygenated functional groups into their precipitate structures. After 20 min of slow mixing, as shown in Fig. 5E, Fe contents remained relatively stable in Fe(II)@PMS and Fe(II)@PS (7.8 % and 10.0 %, respectively), while C content further decreased slightly. The O content remained high across all samples, indicating the sustained formation of iron-enriched oxygenated products through a steady flocculation process.

Fig. S7 illustrates the deconvolution of high-resolution spectra for C1s, O1s, and Fe2p functional groups in NOM (without treatment) and precipitate flocs following various treatment processes. The distribution of functional groups after deconvolution is presented in Fig. 5. Fig. 5B and F show that Fe(II)@SBOs precipitates notably transform from the low degree of oxygenated carbonaceous groups (i.e. C–C/C–H carbon-carbon or C—O alcoholic) to the high degree of oxygenated carbonaceous groups (i.e. C═O and O—C═O) [15]. Differing from Fe(II)@SBOs samples, both C1s profiles of the control NOM and Fe(III) precipitate were comparable, indicating minor modification after coagulation. After rapid mixing, the sum of C—C/C—H and C—O was 82–84 % in the control NOM and Fe(III) precipitate, which reduced to 73 % in Fe(II)@PS and 59 % in Fe(II)@PMS (Fig. 5B). Only Fe(II)@PMS and Fe(II)@PS were able to yield notable degrees of C═O ketone (17–30 %) and newly-formed O—C═O carboxylic groups (10–11 %), likely due to radical-driven oxidation reactions. Compared to Fe(II)@PS, the higher degrees of ketone and carboxylic groups in Fe(II)@PMS were empowered by its stronger capacity in $OH^{\bullet}$ and $SO_4^{\bullet-}$ radical production (Fig. 3), which effectively oxidized NOM into more oxygenated carbon structures. Notably, both C═O and O—C═O in Fe(II)@PMS and Fe(II)@PS disappeared after slow mixing (Fig. 5F), indicating the potential complexation with in situ iron oxide, which may have led to the stabilization and integration of these groups into the precipitate structure.

Further deconvolution of O1s and Fe2p supported the results from C1s. The oxygen-containing functional groups included oxygen lattice O—O, oxygen hydroxyl bond metal O—H, and oxygen chemically or physically absorbed water O–H_2O (Figs. 5C and G) when the iron functional groups were Fe_3O_4, αFe_2O_3, and αFeOOH (Figs. 5D and H) [20,57]. After rapid mixing, both O1s and Fe2p functional groups were comparable among the three samples (Figs. 5C and D). This indicated the initial formation of iron oxide structures, as evident from the brown-yellowish micro-floc images in Figs. 4C **and S5**. However, significant changes were observed after extended mixing time, with increased O—O lattice and Fe_3O_4 contents in Fe(II)@PMS and Fe(II)@PS (Figs. 5G and H). For example, the O—O lattice after slow mixing substantially increased in Fe(II)@PMS (41.7 %) and Fe(II)@PS (56.1 %) relative to Fe(III) (11.7 %) (Fig. 5G). These variations indicated a major shift from hydroxyl groups (O—H) towards strongly bound oxygens in the lattice structure of Fe(II)@SBOs iron-enrich precipitates. This shift strongly correlated to a more well-defined structure of Fe_3O_4 and αFe_2O_3 in Fe(II)@SBOs yielding flocs compared to Fe(III) flocs (Fig. 5H). The expansion of the lattice-ordered framework likely enhanced the complexation between iron oxide with negatively O—C═O carboxylic sites on the NOM surface, as evidenced by the disappearance of carboxylic groups in Fig. 5F. Fe(II)@SBO systems activated NOM through structural

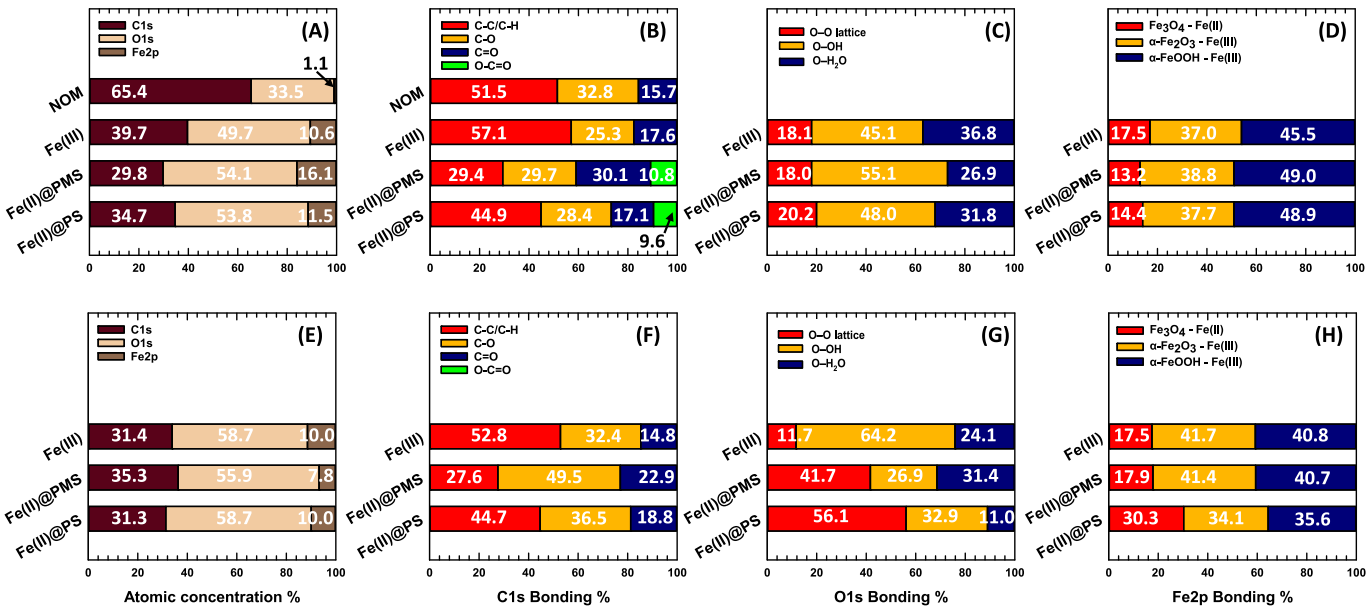

Fig. 5. Atomic composition and transformation of the precipitated products collected from Fe(III), Fe(II)@PMS, and Fe(II)@PS after **(A, B, C, D)** rapid mixing and **(E, F, G, H)** slow mixing. **(A, E)** Elemental atomic concentrations of C1s, O1s, and Fe2p derived from XPS full-scan survey (0–1400 eV); High-resolution XPS survey for oxidation state and chemical functional group characterization of **(B, F)** C1s (300–275 eV), **(C, G)** O1s (545–520 eV), and **(D, H)** Fe2p (740–700 eV). NOM was analyzed as a pristine sample without any treatment.

modification, facilitating lattice-bound oxygen formation with iron oxides. This mechanistic difference resulted in compact, circular precipitates, as opposed to the elongated structures observed in conventional Fe(III) (Fig. 4C).

3.6. Proposed mechanisms and environmental implications

The Fe(II)@SBOs systems leverage the synergic effects of radical generation and in situ coagulation to effectively mitigate NOM-DBP precursors (Fig. 6). First, Fe(II) activates PMS/PS to produce reactive hydroxyl and sulfate radicals. Unlike conventional Fe(III) coagulation, both Fe(II)@SBOs processes tend to transform the carbonaceous structure of NOM rather than facilitating its complete mineralization (Fig. 3). The transformation proceeds quickly after rapid mixing, characterized by a marked reduction in the lower-oxygenated forms (C—C/C—H aromatic and C—O phenolic groups) and corresponding increases in the higher-oxygenated carbonaceous groups (C═O ketone and O—C═O carboxylic groups) (Fig. 5B). This oxidative restructuring contrasts sharply with Fe(III) coagulation, which shows no significant alteration in the carbon functional groups of NOM.

Lower-oxygenated aromatic and phenolic structures exhibit rapid

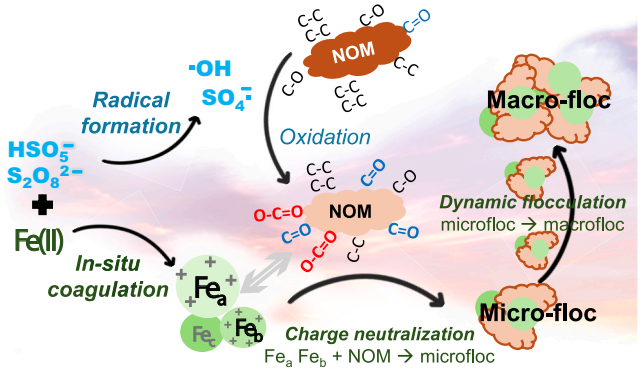

Fig. 6. Proposed dual oxidation-coagulation mechanism for NOM-DBP precursor mitigation in Fe(II)@PMS/PS systems.

chlorination kinetics, with phenolic groups reacting at $k = 10^3$–$10^6 M^{-1} s^{-1}$ (e.g., monohydroxybenzenes and meta-dihydroxybenzenes) [58]. These reactions dominate DBP formation due to the abundance of electron-rich sites. In contrast, higher-oxygenated groups formed during oxidation of Fe(II)@PMS/PS exhibit suppressed reactivity due to electron-withdrawing effects. Aromatic carboxylic acids react with HOCl at $k = 0.1$–$1 M^{-1} s^{-1}$ [59,60], while α,β-unsaturated carbonyl compounds including saturated and unsaturated aldehydes and ketones also undergo slow nucleophilic addition with HOCl at $k = 0.21$–$12 M^{-1} s^{-1}$ [61]. These rate constants for oxidized groups (C═O and O—C═O) are 10–100× slower than those of phenolic precursors (C—C/C—H and C—O), aligning with the typical reactivity of HOCl with electron-deficient functional groups. The oxidized moieties after Fe(II)@PMS/PS reduce electron density at adjacent carbon atoms through inductive and resonance effects, diminishing chlorine electrophilic attack. This electron-deactivation by Fe@SBOs likely transforms the NOM from a highly reactive DBP precursor material into a less reactive, more oxidized form, consequently reducing the overall DBP formation.

Complementing this oxidation process, the newly formed oxygenated functional groups exhibit a strong affinity for in situ iron oxides. In situ Fe(III) features hydroxylated monomeric and oligomeric Fe(III) species (e.g., $Fe(OH)_2^+$, $Fe_2(OH)_2^{4+}$), which enhance charge neutralization and promote swift micro-floc formation (Fig. 4B). This process generates smaller, denser, and more regularly shaped flocs compared to conventional Fe(III) coagulation (Fig. 4C), improving hydraulic sweep efficiency and enabling >70 % removal of oxidized NOM during sedimentation (Fig. 4A). Carboxylic acids, in particular, can form stable complexes with Fe(III)-oxyhydroxides (e.g., Fe—O(—COO—) with a binding length of 1.80 Å [62]), enabling better removal of oxidized NOM after slow mixing. Zhou et al. [63] and Fizer et al. [64] have demonstrated that carboxyl and phenolic groups serve as the primary binding sites for Fe(III) with humic substances, which aligns closely with our XPS findings related to the formation and consumption of O—C═O functionalities during flocculation. This is evidenced by the complete disappearance of O—C═O groups in post-treatment precipitates (Fig. 5F). Concurrently, the magnetite (Fe_3O_4) and hematite (αFe_2O_3) becomes dominant in Fe(II)@PMS/PS systems, with the O—O lattice structure increasing by 30–45 % compared to Fe(III) controls (Figs. 5G

and 5H). The dual mechanisms of Fe(II)@PMS/PS, with radical-driven oxidation followed by thermodynamically favored complexation, achieves ~90 % DBP precursor removal at optimal doses, outperforming Fe (III) coagulation, which relies solely on electrostatic neutralization and achieves only 55–77 % reduction (Fig. 3A).

Bliss Independence Model was used to quantify the synergistic interactions, yielding indices of 0.93–0.97 based on the DOC removal metrics among the control with the scavenging and chelating experiments. However, this single-parameter approach could not capture the multifaceted synergy in Fe@SBOs, as coordinated molecular transformations, enhanced iron speciation, and improved floc characteristics all involve. Our synergy is based on mechanistic integration rather than simple additive effects, which requires further advancement in quantitative frameworks for multi-mechanism water treatment processes.

The substantial reduction in cytotoxicity index values (0.5–1 order of magnitude lower than raw water, Fig. 3B) demonstrates the environmental superiority of Fe(II)@PMS/PS systems over conventional Fe(III). While this study focused on 1–2 carbon volatile DBPs (e.g., TCM, DCAN), the observed suppression of electron-rich precursor sites and enhanced removal of oxidized NOM strongly suggests analogous reductions in haloacetic acids (HAAs) and other unregulated DBPs. The smaller, denser flocs generated by Fe(II)-activated systems are expected to improve sedimentation efficiency. The dual oxidation-coagulation mechanism addresses both regulated and emerging DBPs while mitigating risks associated with chlorinated byproduct persistence in aquatic ecosystems. This positions Fe(II)@PMS/PS as a scalable strategy for balancing water safety, treatment sustainability, and infrastructure resilience in NOM-rich water sources.

4. Conclusion

This study demonstrates that Fe(II)-activated sulfate-based oxidation systems (Fe(II)@PMS/PS) significantly outperform conventional Fe(III) coagulation through a novel dual mechanism combining radical oxidation with dynamic in-situ coagulation. Fe(II)@PMS/PS generates $^{\bullet}OH$ and $SO_4^{\bullet-}$ radicals, which oxidize electron-rich NOM structures (aromatic C—C/C—H and phenolic C—O groups) into highly oxygenated configurations (ketones C═O and carboxylic acids O—C═O groups). The process transforms electron-rich NOM precursors into oxidized, less chlorine-reactive forms while simultaneously generating compact Fe (III) flocs. The hydroxylated monomeric/polymeric species dominates the formation of in-situ Fe(III), enhancing rapid charge neutralization and micro-floc formation. Fe(II)@PMS/PS reduces 80–90 % DBP precursor removal compared to 55–77 % for conventional coagulation, eventually lowering cytotoxicity risks by 0.5–1 order of magnitude. The Fe(II)@PMS/PS systems offer a promising single-step solution for organic-rich source waters, while simultaneously addressing both precursor reactivity modification and physical removal—a significant advancement over existing technologies that rely primarily on physical separation mechanisms.

CRediT authorship contribution statement

Lap-Cuong Hua: Writing – review & editing, Writing – original draft, Visualization, Validation, Supervision, Project administration, Methodology, Investigation, Formal analysis, Data curation, Conceptualization. **Yosheng Lin:** Writing – original draft, Visualization, Validation, Software, Methodology, Investigation, Formal analysis, Data curation. **Thi Ngoc Anh Nguyen:** Visualization, Validation, Software, Methodology, Investigation, Formal analysis, Data curation. **Jr Lin Lin:** Validation, Software, Methodology, Investigation, Formal analysis, Data curation. **Chihpin Huang:** Writing – review & editing, Supervision, Resources, Project administration, Investigation, Funding acquisition, Conceptualization.

Declaration of competing interest

The authors declare that they have no known competing financial interests or personal relationships that could have appeared to influence the work reported in this paper.

Acknowledgments

We thank the National Science and Technology Council of Taiwan (MOST 111-2221-E-A49-007-MY3) for the financial support. We also thank the Instrumentation Centre at National Tsing Hua University (NTHU) for providing the EPR analysis facility.

Appendix A. Supplementary data

Supplementary data to this article can be found online at https://doi.org/10.1016/j.seppur.2025.135378.

Data availability

No data was used for the research described in the article.

References

[1] H. Daraei, E. Bertone, R.A. Stewart, J. Awad, A. Leavesley, M. Gale, E. Jones, K. Cinque, M. Agnew, H.A. Burger, J. Van Leeuwen, Organic matter concentration and characteristic dynamics in surface waters post-bushfires and cyclones: fDOM sensors for environmental monitoring and control, Environ. Sci. Adv. 3 (6) (2024) 950–963.
[2] T. Maqbool, Y. Qin, Q.V. Ly, J. Zhang, C. Li, M.B. Asif, Z. Zhang, Exploring the relative changes in dissolved organic matter for assessing the water quality of full-scale drinking water treatment plants using a fluorescence ratio approach, Water Res. 183 (2020) 116125.
[3] L.-C. Hua, S.-J. Chao, K. Huang, C. Huang, Characteristics of low and high SUVA precursors: relationships among molecular weight, fluorescence, and chemical composition with DBP formation, Sci. Total Environ. 727 (2020) 138638.
[4] J. Li, Y. Song, J. Jiang, T. Yang, Y. Cao, Oxidative treatment of NOM by selective oxidants in drinking water treatment and its impact on DBP formation in postchlorination, Sci. Total Environ. 858 (2023) 159908.
[5] L.-C. Hua, C.-H. Lai, G.-S. Wang, T.-F. Lin, C. Huang, Algogenic organic matter derived DBPs: precursor characterization, formation, and future perspectives – A review, Crit. Rev. Environ. Sci. Technol. 49 (19) (2019) 1803–1834.
[6] L. Önnby, E. Salhi, G. McKay, F.L. Rosario-Ortiz, U. von Gunten, Ozone and chlorine reactions with dissolved organic matter - assessment of oxidant-reactive moieties by optical measurements and the electron donating capacities, Water Res. 144 (2018) 64–75.
[7] R. Wang, M. Ji, H. Zhai, Y. Liang, Electron donating capacities of DOM model compounds and their relationships with chlorine demand, byproduct formation, and other properties in chlorination, Chemosphere 261 (2020) 127764.
[8] D. Wang, X. Chen, J. Luo, P. Shi, Q. Zhou, A. Li, Y. Pan, Comparison of chlorine and chlorine dioxide disinfection in drinking water: evaluation of disinfection byproduct formation under equal disinfection efficiency, Water Res. 260 (2024) 121932.
[9] W.A. Mitch, S.D. Richardson, X. Zhang, M. Gonsior, High-molecular-weight by-products of chlorine disinfection, Nat. Water 1 (4) (2023) 336–347.
[10] Richardson, S.D. and Postigo, C., pp. 1–18, Springer Berlin Heidelberg, Berlin, Heidelberg.
[11] M. Valenti-Quiroga, M.J. Farré, P. Roccaro, Upgrading water treatment trains to comply with the disinfection by-products standards introduced by the directive (EU) 2020/2184, Curr. Opin. Environ. Sci. Health 39 (2024) 100547.
[12] C.M. Villanueva, I. Evlampidou, F. Ibrahim, C. Donat-Vargas, A. Valentin, A.-M. Tugulea, S. Echigo, D. Jovanovic, A.T. Lebedev, M. Lemus-Pérez, M. Rodriguez-Susa, A. Luzati, T. de Cássia dos Santos Nery, P.A. Pastén, M. Quiñones, S. Regli, R. Weisman, S. Dong, M. Ha, S. Phattarapattamawong, T. Manasfi, S.-I.E. Musah, A. Eng, K. Janák, S.C. Rush, D. Reckhow, S.W. Krasner, P. Vineis, S.D. Richardson, M. Kogevinas, Global assessment of chemical quality of drinking water: the case of trihalomethanes, Water Res. 230 (2023) 119568.
[13] H. Dong, A.A. Cuthbertson, M.J. Plewa, C.R. Weisbrod, A.M. McKenna, S. D. Richardson, Unravelling high-molecular-weight DBP toxicity drivers in chlorinated and Chloraminated drinking water: effect-directed analysis of molecular weight fractions, Environ. Sci. Technol. 57 (47) (2023) 18788–18800.
[14] S.D. Richardson, M.J. Plewa, To regulate or not to regulate? What to do with more toxic disinfection by-products? J. Environ. Chem. Eng. 8 (4) (2020) 103939.
[15] L.-C. Hua, C. Huang, C. Huang, Insights on free radical oxidation and in-situ coagulation in PMS/Fe(II) process for the removal of algogenic organic matter precursors, Chem. Eng. J. 446 (2022) 136986.
[16] J.-L. Lin, A.R. Ika, Minimization of halogenated DBP precursors by enhanced PACl coagulation: the impact of organic molecule fraction changes on DBP precursors destabilization with Al hydrates, Sci. Total Environ. 703 (2020) 134936.

[17] M.-H. Tsai, L.-C. Hua, K. Huang, C. Huang, NOM removal and residual Al minimization by enhanced coagulation: roles of sequence dosing with PACl–FeCl3, J. Water Supply Res. Technol. AQUA 69 (6) (2020) 616–628.
[18] P. Wang, S. Ding, R. Xiao, G. An, C. Fang, W. Chu, Enhanced coagulation for mitigation of disinfection by-product precursors: A review, Adv. Colloid Interf. Sci. 296 (2021) 102518.
[19] Y. Jathan, K.R. Pagilla, E.A. Marchand, Understanding the influence of dissolved organic nitrogen characteristics on enhanced coagulation performance for water reuse, Chemosphere 337 (2023) 139384.
[20] L.-C. Hua, R.-C. OuYang, Z. Zhao, T.N.A. Nguyen, C. Huang, Homogeneous versus heterogeneous Mn(II) oxidation in Peroxymonosulfate assisting chlorination: synergistic role for enhanced Mn(II) oxidation in water treatment, Water Res. (2024) 122265.
[21] B. Yang, N. Graham, P. Liu, M. Liu, J. Gregory, W. Yu, Atomic-level structural differences between Fe(III) Coprecipitates generated by the addition of Fe(III) coagulants and by the oxidation of Fe(II) coagulants determine their coagulation behavior in phosphate and DOM removal, Environ. Sci. Technol. 57 (33) (2023) 12489–12500.
[22] J. Zhou, J. Liu, Z. Zhao, W. Peng, F. Cui, Z. Liang, Microcystis aeruginosa-laden water treatment using peroxymonosulfate enhanced Fe(II) coagulation: performance and the role of in situ formed Fe3O4, Chem. Eng. J. 382 (2020) 123012.
[23] S. Giannakis, K.-Y.A. Lin, F. Ghanbari, A review of the recent advances on the treatment of industrial wastewaters by sulfate radical-based advanced oxidation processes (SR-AOPs), Chem. Eng. J. 406 (2021) 127083.
[24] L. McGachy, D.L. Sedlak, From theory to practice: leveraging chemical principles to improve the performance of Peroxydisulfate-based in situ chemical oxidation of organic contaminants, Environ. Sci. Technol. 58 (1) (2024) 17–32.
[25] J. Wang, S. Wang, Activation of persulfate (PS) and peroxymonosulfate (PMS) and application for the degradation of emerging contaminants, Chem. Eng. J. 334 (2018) 1502–1517.
[26] X. Hu, M. Zhu, Were persulfate-based advanced oxidation processes really understood? Basic concepts, cognitive biases, and experimental details, Environ. Sci. Technol. 58 (24) (2024) 10415–10444.
[27] Y. Yan, Z. Wei, X. Duan, M. Long, R. Spinney, D.D. Dionysiou, R. Xiao, P.J. J. Alvarez, Merits and limitations of radical vs. nonradical pathways in persulfate-based advanced oxidation processes, Environ. Sci. Technol. 57 (33) (2023) 12153–12179.
[28] M. Liu, N. Graham, J. Gregory, M. Elimelech, W. Yu, Towards a molecular-scale theory for the removal of natural organic matter by coagulation with trivalent metals, Nat. Water 2 (3) (2024) 285–294.
[29] M.-H. Tsai, W.-L. Liang, L.-C. Hua, C. Huang, Influence of Al/Fe-based coagulant dosing sequences on floc formation and settling behavior in algae-laden water, Environ. Sci.: Water Res. Technol. 8 (1) (2022) 127–138.
[30] R. Pan, Y. Huang, J. Ao, Y. Wu, L. Bu, S. Zhou, L. Deng, Z. Shi, A molecular-level mechanism analysis of PFS coagulation behaviors: Differences in natural organic matter and algal organic matter, Separation and Purification Technology 314 (2023) 123485, https://doi.org/10.1016/j.seppur.2023.123485.
[31] B. Yang, S. Rashid, N. Graham, W. Yu, The impact of small organic molecules on Fe (II) coagulation: facilitating vs. shielding mechanisms on charge transfer, Sep. Purif. Technol. 323 (2023) 124424.
[32] L.-C. Hua, J.-L. Lin, M.-Y. Syue, C. Huang, P.-C. Chen, Optical properties of algogenic organic matter within the growth period of Chlorella sp. and predicting their disinfection by-product formation, Sci. Total Environ. 621 (2018) 1467–1474.
[33] C. Liang, C.-F. Huang, N. Mohanty, R.M. Kurakalva, A rapid spectrophotometric determination of persulfate anion in ISCO, Chemosphere 73 (9) (2008) 1540–1543.
[34] T. Chen, S. Dong, X. Guo, W. Chu, T. Xu, D. Yin, Dissolved organic carbon removal and CX3R-type byproduct formation during the peroxymonosulfate pre-oxidation followed by coagulation, Chem. Eng. J. 421 (2021) 129654.
[35] J. Lee, U. von Gunten, J.-H. Kim, Persulfate-based advanced oxidation: critical assessment of opportunities and roadblocks, Environ. Sci. Technol. 54 (6) (2020) 3064–3081.
[36] Y. Li, Y. Pan, L. Lian, S. Yan, W. Song, X. Yang, Photosensitized degradation of acetaminophen in natural organic matter solutions: the role of triplet states and oxygen, Water Res. 109 (2017) 266–273.
[37] Y. Gao, D. Wang, Y. Zhang, M. Yang, Characterization of hydrolyzed Fe(III) species produced in Fenton's reaction, Environ. Technol. 30 (14) (2009) 1585–1591.
[38] B. Lan, C. Hao, M. Zhang, X. Yan, Diverse performances for Pb(II) adsorption by in situ formed Fe(III) oxyhydroxide derived from ferrate(VI) reduction and ferrous oxidation, Environ. Sci. Pollut. Res. 30 (31) (2023) 77488–77498.
[39] P.A. Moussas, A.I. Zouboulis, Synthesis, characterization and coagulation behavior of a composite coagulation reagent by the combination of polyferric sulfate (PFS) and cationic polyelectrolyte, Sep. Purif. Technol. 96 (2012) 263–273.
[40] C. Feng, B. Shi, D. Wang, G. Li, H. Tang, Characteristics of simplified Ferron colorimetric solution and its application in hydroxy-aluminum speciation, Colloids Surf. A Physicochem. Eng. Asp. 287 (1) (2006) 203–211.
[41] L.-C. Hua, C. Huang, Y.-C. Su, T.-N.-P. Nguyen, P.-C. Chen, Effects of electro-coagulation on fouling mitigation and sludge characteristics in a coagulation-assisted membrane bioreactor, J. Membr. Sci. 495 (2015) 29–36.
[42] D.N.G. Ngo, X.-Y. Chuang, C.-P. Huang, L.-C. Hua, C. Huang, Compositional characterization of nine agricultural waste biochars: the relations between alkaline metals and cation exchange capacity with ammonium adsorption capability, J. Environ. Chem. Eng. 11 (3) (2023) 110003.
[43] L.-C. Hua, S.R. Tsia, G.-S. Wang, C.-D. Dong, C. Huang, Increasing bromine in intracellular organic matter of freshwater algae growing in bromide-elevated environments and its impacts on characteristics of DBP precursors, Environ. Sci. Technol. Lett. 8 (4) (2021) 307–312.
[44] A. Rastogi, S.R. Al-Abed, D.D. Dionysiou, Effect of inorganic, synthetic and naturally occurring chelating agents on Fe(II) mediated advanced oxidation of chlorophenols, Water Res. 43 (3) (2009) 684–694.
[45] Z. Yang, Y. Cui, B. Pan, J.J. Pignatello, Peroxymonosulfate activation by Fe(III)–Picolinate complexes for efficient water treatment at Circumneutral pH: Fe(III)/Fe (IV) cycle and generation of Oxyl radicals, Environ. Sci. Technol. 57 (47) (2023) 18918–18928.
[46] X. Liu, S. Ding, P. Wang, Y. Hong, H. Zhao, W. Chu, Simultaneous mitigation of disinfection by-product formation and odor compounds by peroxide/Fe(II)-based process: combination of oxidation and coagulation, Water Res. 201 (2021) 117327.
[47] J. Mo, T. Lin, X. Zhang, F. Jiang, H. Chen, Effects of Fe(II)-activated persulfate/sodium percarbonate (PS/SPC) pretreatment on ultrafiltration membrane fouling control and mechanisms, Desalination 547 (2023) 116258.
[48] Y. Wei, K. Li, P. Li, Z. Guo, R. Shi, H. Zhao, T. Sun, C. Zhou, Enhanced ceramic membranes filtration by PS pre-oxidation with CuO assisted FeSO4 catalytic for NOM removal in drinking water treatment, Sep. Purif. Technol. 345 (2024) 127333.
[49] X. Wei, M. Yang, Q. Zhu, E.D. Wagner, M.J. Plewa, Comparative quantitative toxicology and QSAR modeling of the Haloacetonitriles: forcing agents of water disinfection byproduct toxicity, Environ. Sci. Technol. 54 (14) (2020) 8909–8918.
[50] S.S. Lau, Y. Feng, A.Z. Gu, C. Russell, G. Pope, W.A. Mitch, Cytotoxicity comparison between drinking water treated by chlorination with Postchloramination versus granular activated carbon (GAC) with Postchlorination, Environ. Sci. Technol. 57 (36) (2023) 13699–13709.
[51] E.D. Wagner, M.J. Plewa, CHO cell cytotoxicity and genotoxicity analyses of disinfection by-products: An updated review, J. Environ. Sci. 58 (2017) 64–76.
[52] Y. Chen, H.C. Vu, C.J. Miller, S. Garg, D. Pan, T.D. Waite, Comparative experimental and computational studies of hydroxyl and sulfate radical-mediated degradation of simple and complex organic substrates, Environ. Sci. Technol. 56 (12) (2022) 8819–8832.
[53] G.V. Buxton, C.L. Greenstock, W.P. Helman, A.B. Ross, Critical review of rate constants for reactions of hydrated electrons, hydrogen atoms and hydroxyl radicals (·OH/·O−) in aqueous solution, J. Phys. Chem. Ref. Data Monogr. 17 (2) (1988) 513–886.
[54] P. Neta, R.E. Huie, A.B. Ross, Rate constants for reactions of inorganic radicals in aqueous solution, J. Phys. Chem. Ref. Data Monogr. 17 (3) (1988) 1027–1284.
[55] D. Rao, H. Dong, M. Niu, X. Wang, J. Qiao, Y. Sun, X. Guan, Mechanistic insights into the markedly decreased oxidation capacity of the Fe(II)/S2O82– process with increasing pH, Environ. Sci. Technol. 56 (18) (2022) 13131–13141.
[56] T. Hong-Xiao, W. Stumm, The coagulating behaviors of Fe(III) polymeric species—I. Preformed polymers by base addition, Water Res. 21 (1) (1987) 115–121.
[57] Y.-L. Chen, L.-C. Hua, M.-H. Tsai, T.-Y. Chien, C. Huang, Chemisorption of fluoride onto manganese-oxide-coated activated alumina in aqueous solution, J. Hazard. Mater. Adv. 6 (2022) 100095.
[58] H. Gallard, U. von Gunten, Chlorination of phenols: kinetics and formation of chloroform, Environ. Sci. Technol. 36 (5) (2002) 884–890.
[59] D.I. Pattison, M.J. Davies, Absolute rate constants for the reaction of Hypochlorous acid with protein side chains and peptide bonds, Chem. Res. Toxicol. 14 (10) (2001) 1453–1464.
[60] T. Zhang, U. von Gunten, Chlorination of amides: kinetics and mechanisms of formation of N-chloramides and their reactions with phenolic compounds, Water Res. 242 (2023) 120131.
[61] E.L. Marron, J. Van Buren, A.A. Cuthbertson, E. Darby, U. von Gunten, D.L. Sedlak, Reactions of α,β-Unsaturated Carbonyls with Free Chlorine, Free Bromine, and Combined Chlorine, Environ. Sci. Technol. 55 (5) (2021) 3305–3312.
[62] T. Zhang, Z. Pan, J. Wang, X. Qian, H. Yamashita, Z. Bian, Y. Zhao, Homogeneous carbon dot-anchored Fe(III) catalysts with self-regulated proton transfer for recyclable Fenton chemistry, JACS Au 3 (2) (2023) 516–525.
[63] P. Zhou, H. Yan, B. Gu, Competitive complexation of metal ions with humic substances, Journal of Colloid and Interface Science 283 (2) (2005) 383–389, https://doi.org/10.1016/j.jcis.2004.09.046.
[64] M. Fizer, V. Sidey, S. Milyovich, O. Fizer, A DFT study of fulvic acid binding with bivalent metals: Cd, Cu, Mg, Ni, Pb, Zn, J. Mol. Graph. Model. 102 (2021) 107800.